



## The design of strut/TPMS-based pore geometries in bioceramic scaffolds guiding osteogenesis and angiogenesis in bone regeneration



Yifan Li<sup>a,1</sup>, Jiafeng Li<sup>a,1</sup>, Shuai Jiang<sup>a</sup>, Cheng Zhong<sup>a</sup>, Chenchen Zhao<sup>a</sup>, Yang Jiao<sup>a</sup>, Jian Shen<sup>a</sup>, Huaizhi Chen<sup>a</sup>, Meihan Ye<sup>a</sup>, Jiayu Zhou<sup>c</sup>, Xianyan Yang<sup>b</sup>, Zhongru Gou<sup>b,\*\*\*</sup>, Sanzhong Xu<sup>a,\*\*</sup>, Miaoda Shen<sup>a,\*</sup>

<sup>a</sup> Department of Orthopedics, The First Affiliated Hospital, Zhejiang University School of Medicine, Hangzhou, 310003, PR China

<sup>b</sup> Bio-nanomaterials and Regenerative Medicine Research Division, Zhejiang-California International Nanosystem Institute, Zhejiang University, Hangzhou, 310058, PR China

<sup>c</sup> Affiliated Mental Health Centre & Hangzhou Seventh People's Hospital, Zhejiang University School of Medicine, Hangzhou, 310013, PR China

### ARTICLE INFO

#### Keywords:

Wollastonite bioceramics  
Pore geometry  
Osteogenesis  
Angiogenesis  
Triply periodic minimal surfaces

### ABSTRACT

The pore morphology design of bioceramic scaffolds plays a substantial role in the induction of bone regeneration. Specifically, the effects of different scaffold pore geometry designs on angiogenesis and new bone regeneration remain unclear. Therefore, we fabricated Mg/Sr co-doped wollastonite bioceramic (MS-CSi) scaffolds with three different pore geometries (gyroid, cylindrical, and cubic) and compared their effects on osteogenesis and angiogenesis *in vitro* and *in vivo*. The MS-CSi scaffolds were fabricated by digital light processing (DLP) printing technology. The pore structure, mechanical properties, and degradation rate of the scaffolds were investigated. Cell proliferation on the scaffolds was evaluated using CCK-8 assays while angiogenesis was assessed using Transwell migration assays, tube formation assays, and immunofluorescence staining. The underlying mechanism was explored by western blotting. Osteogenic ability of scaffolds was evaluated by alkaline phosphatase (ALP) staining, western blotting, and qRT-PCR. Subsequently, a rabbit femoral defect model was prepared to compare differences in the scaffolds in osteogenesis and angiogenesis *in vivo*. Cell culture experiments showed that the gyroid pore scaffold downregulated YAP/TAZ phosphorylation and enhanced YAP/TAZ nuclear translocation, thereby promoting proliferation, migration, tube formation, and high expression of CD31 in human umbilical vein endothelial cells (HUVECs) while strut-based (cubic and cylindrical pore) scaffolds promoted osteogenic differentiation in bone marrow mesenchymal stem cells and upregulation of osteogenesis-related genes. The gyroid pore scaffolds were observed to facilitate early angiogenesis in the femoral-defect model rabbits while the strut-based scaffolds promoted the formation of new bone tissue. Our study indicated that the pore geometries and pore curvature characteristics of bioceramic scaffolds can be precisely tuned for enhancing both osteogenesis and angiogenesis. These results may provide new ideas for the design of bioceramic scaffolds for bone regeneration.

### 1. Introduction

Bone tissue engineering scaffolds represent a promising treatment option as they avoid problems such as the limited availability and immunogenicity of autologous bone, and the morbidity associated with

donor placement [1,2]. Bioceramic scaffolds with optimal physical-chemical and biological properties are potential candidates for promoting bone regeneration [3–5]. Many studies have used bioceramic scaffolds as an alternative to bone grafting but the results are often unsatisfactory. Pore geometry design may be a strategy for the development

\* Corresponding author. Department of Orthopedics, the First Affiliated Hospital Zhejiang University School of Medicine, #79 Qingchun Road, Hangzhou, Zhejiang Province, 310003, PR China.

\*\* Corresponding author. Department of Orthopedics, the First Affiliated Hospital Zhejiang University School of Medicine, #79 Qingchun Road, Hangzhou, Zhejiang Province, 310003, PR China.

\*\*\* Corresponding author. Zhejiang-California International Nanosystems Institute Zhejiang University, #866 Yuhangtang Road, Hangzhou, Zhejiang Province, 310058, PR China.

E-mail addresses: [zhrgou@zju.edu.cn](mailto:zhrgou@zju.edu.cn) (Z. Gou), [xusanzhong@zju.edu.cn](mailto:xusanzhong@zju.edu.cn) (S. Xu), [mds@zju.edu.cn](mailto:mds@zju.edu.cn) (M. Shen).

<sup>1</sup> Co-first author.

of bioceramic scaffolds with superior properties for the promotion of bone regeneration. Furthermore, increasing numbers of studies have recognized that the pore geometries of scaffolds also affect the efficiency of cell migration and tissue regeneration [6–8].

Ca-silicate biomaterials have potential as bone implants because of their superior biocompatibility and ability to stimulate osteogenesis [9–11]. However, the rapid rate of biodegradation and suboptimal strength of pure wollastonite (CSi) bioceramic prevent its meeting the structural requirements of various types of bone defects [12]. Therefore, the incorporation of functional ions with CSi has attracted much attention. Our previous study found that doping with dilute magnesium modulated the mechanical properties and biodegradation rate of CSi [13]. Some researchers have also found that strontium could promote the adhesion, proliferation, and differentiation of bone marrow-derived mesenchymal stem cells (BMSCs) on CSi [14,15]. In addition, strontium can promote bone formation by promoting osteoprotegerin synthesis and suppressing the production of macrophage colony-stimulating factor in BMSCs [16]. Magnesium/strontium co-doped CSi (MS-CSi) scaffolds fabricated using a direct ink-writing technique have acceptable compressive strength and appreciable osteogenic activity compared with  $\beta$ -TCP and magnesium-doped CSi (M-CSi) scaffolds [17]. The use of MS-CSi scaffolds can overcome the problem of premature degradation and allows the release of ions during immersion. Furthermore, such scaffolds can also stimulate the AKT and WNT signaling pathways to regulate bone regeneration [18]. Most recently, we have prepared the MS-CSi scaffolds by using digital light printing (DLP), and preliminary results have shown that variations in the magnesium/strontium ratio can modulate the mechanical properties and biodegradation of the scaffolds [19]. We have also found that the pore size had a significant effect on the osteoconductive efficiency of the CSi scaffolds [20]. Therefore, it is reasonable to consider that DLP can accurately fabricate MS-CSi scaffolds with complex biomimetic structures.

There is currently much research into how to fabricate triperiodic minimal surface (TPMS)-type porous scaffolds with different structural properties [21–24]. TPMS has a continuous surface that supports osteoblast implantation, a controllable pore diameter that can balance angiogenesis and load-bearing in regenerated bone, and its zero mean curvature is similar to that of natural bone trabeculae [25–27]. Additionally, it alleviates the concentration of stress compared with strut scaffolds formed of straight struts connected to joints [28]. Specifically, the gyroid pore architecture is considered to have excellent fluid permeability and mechanical properties [29–31]. Theoretically, it would appear to have an ideal pore geometry for promoting bone regeneration. However, there are few studies on the effects and differences between strut- and TPMS-based porous bioceramics on the osteogenic and angiogenic behavior of cells. Thus, it is of great importance for the development of bioceramic scaffolds to understand the relationship between pore geometry and favorable osteogenesis and/or angiogenesis [32,33].

Based on the perspective described above, MS-CSi scaffolds with three different pore geometries, namely, gyroid, cylindrical, and cubic pores, were fabricated using DLP technology. The structural parameters of the different scaffolds were compared by Micro-CT and scanning electron microscopy (SEM). The mechanical properties and degradation of the scaffolds were analyzed by *in vitro* immersion experiments. The effects of these designed scaffolds on osteogenesis and angiogenesis and the underlying mechanisms were investigated both *in vitro* and *in vivo*. The gyroid pore scaffolds increased proliferation, migration, tube formation and expression of CD31 of human umbilical vein endothelial cells (HUVECs) by enhancing mechanical signaling through the YAP/TAZ pathway. Expression of osteogenesis-related genes was significantly enhanced in the cubic and cylindrical pore scaffolds. The different scaffolds also showed different osteogenic and angiogenic trends *in vivo*. Therefore, it is of significant importance to clarify the structural characteristics of pores that can facilitate the development of a safer and more

effective scaffold for bone regeneration in clinical applications. In this regard, the present study will provide guidance for the use of multi-functional scaffolds that promote both osteogenesis and angiogenesis.

## 2. Materials and methods

### 2.1. Synthesis and characterization of MS-CSi powders

The MS-CSi powder with 6% Mg- and 3% Sr-substituting-Ca was synthesized by a wet-chemical co-precipitation method as described previously [13]. A crystallographic analysis of the powder sample was performed using X-ray diffraction (XRD; Rigaku, Japan). The chemical composition of bioceramic powder was determined by inductively coupled plasma optical emission spectroscopy (ICP-OES; 710-ES, Varian; USA).

### 2.2. Fabrication of scaffolds with different pore geometries

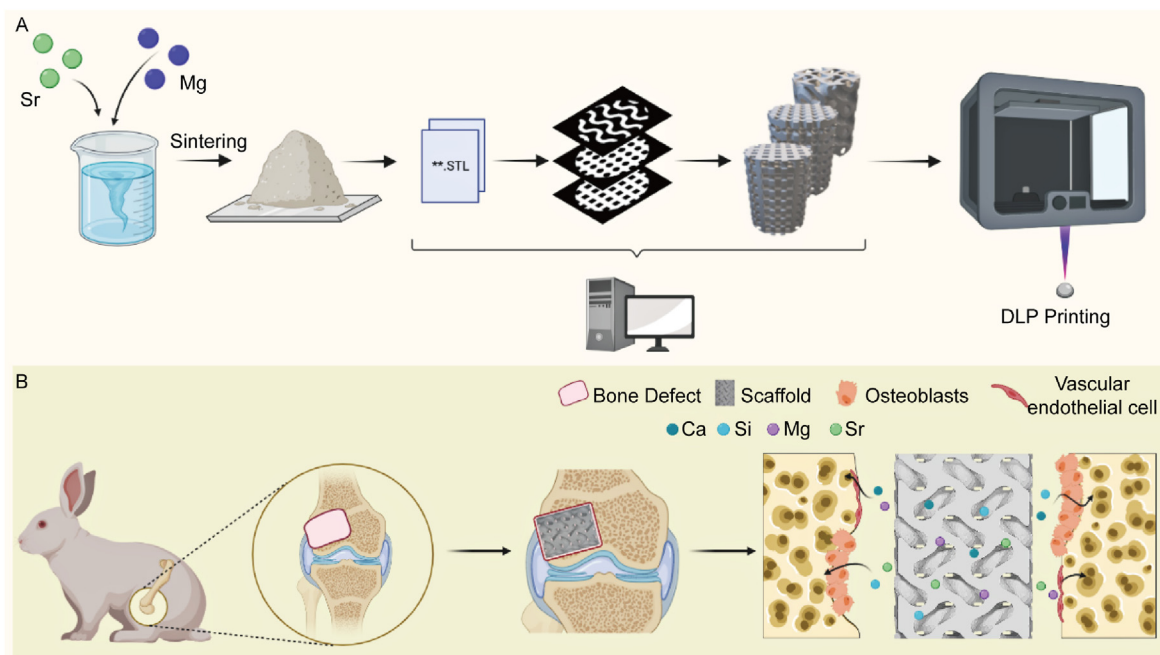
Porous scaffold models ( $\varnothing 6 \times 8$  mm) with different pore geometries (i.e., cubic, cylindrical, and gyroid geometries; see Scheme 1A) were designed by Magics software (version 21, Materialise, Leuven, Belgium) as described previously [19]. All scaffolds had a designed porosity of ~55% and a designed average pore size of ~600  $\mu\text{m}$  which was calculated by Avizo Software (FEI VSG, Hillsboro OR, USA). Detailed information about the method and the process can be found in our previous study [34]. The scaffold models were exported as binary STL format files, which were imported into 10dim software (Ten Dimensions Technology Co. Ltd., China) for supporting generation and slicing. The green bodies were printed in a 3D printer (AUTOCERA-M, Ten Dimensions Technology Co. Ltd., China) by the slurry containing the MS-CSi powders and printing resins (MS-CSi Powder 60 wt%) according to STL files. The green bodies were sintered in a muffle furnace at a target temperature of 1150  $^{\circ}\text{C}$  for 3 h.

### 2.3. Macroscopic geometry assay of scaffolds

The gross geometry of porous scaffolds was observed using an optical microscope (DM2500, Leica, Germany). The scale and connectivity of internal pores were evaluated by micro-computed tomography (Micro-CT; Inveon TM CT scanner, Siemens, Germany). The porosity, pore diameter, pore wall thickness, and specific surface area of scaffolds were also calculated by Micro-CT. The structure and pore geometry on the surface of scaffolds were observed by SEM (GEMINI 300, ZEISS, Germany).

### 2.4. Mechanical and biodegradation properties assay *in vitro*

For evaluation of mechanical properties, the compressive strength of bioceramic scaffolds ( $\varnothing 6.0 \times 8.0$  mm) was tested by the universal testing machine (5566, Instron, Japan). An initial linear region of the stress-strain curves was used to measure the Young's modulus. The scaffolds were weighed and then immersed in Tris-HCl buffer for evaluation of biodegradation *in vitro*. The scaffold samples were removed at predetermined intervals (1, 2, 4, 8, 12 weeks) and washed with absolute ethanol before being dried at 80  $^{\circ}\text{C}$  for 12 h before mass loss calculations were performed. Following immersion for 1, 3, 5, 7, 14 days, the buffer (1.0 mL) was extracted for ICP analysis of the released ionic concentrations (Si, Ca, Mg, Sr), and equivalent fresh buffer was added to the immersion medium. Additionally, the biomimetic re-mineralization (bioactivity *in vitro*) of scaffolds was evaluated after 7 days of immersion in simulated body fluid (SBF) was carried out using SEM and energy dispersive spectroscopy (EDS) techniques to examine the apatite formation on scaffold surfaces.



**Scheme 1.** (A) Diagram of the DLP technology of fabricating MS-CSi bioceramics. (B) Diagram of scaffolds implanting into rabbit femoral defect and promoting bone repair by releasing functional ions (Created with BioRender.com).

## 2.5. Biocompatibility assay *in vitro*

### 2.5.1. Cell culture

HUVECs and rat bone marrow mesenchymal stem cells (BMSCs) were used respectively for the *in vitro* study. HUVECs were purchased from the American Type Culture Collection (Manassas, USA) and cultured in a high-glucose Dulbecco's Modified Eagle's Medium (DMEM, HyClone, USA) supplemented with the 10% fetal bovine serum (FBS, HyClone, USA) and 1% penicillin/streptomycin (Gibco, USA) in a 5% CO<sub>2</sub> humidified atmosphere at 37 °C. The culture medium was replaced every two days. BMSCs were isolated from the femur and tibia of Sprague-Dawley (SD) rats and cultured with complete  $\alpha$ -MEM. Culture methods for BMSCs are similar to those used for HUVECs. BMSCs from passages 3–4 were used in subsequent studies.

### 2.5.2. Cell proliferation assay

BMSCs and HUVECs were seeded onto the scaffolds ( $n = 6$ ) at a density of  $1 \times 10^3$  cells/L. A cell counting kit-8 (CCK-8; Biosharp, China) was used to determine cell proliferation after 1, 3, and 7 days of culture. After washing the cells twice in PBS, fresh medium (300  $\mu$ L) and CCK-8 solution (30  $\mu$ L) were added to the wells, followed by incubation at 37 °C for 2 h. Lastly, 100  $\mu$ L of the supernatant was transferred to a 96-well plate and the absorbance at 450 nm was measured to detect cell proliferation.

### 2.5.3. Transwell migration assay

A Transwell migration assay was conducted using Transwell cell culture inserts (8  $\mu$ m pore size, Corning Costar; USA) to assess the vertical migration of HUVECs. Briefly, HUVECs ( $1 \times 10^5$  cells/mL) were cocultured on scaffolds for 48 h and then resuspended and seeded in the upper chamber with FBS-free DMEM, while the lower chamber contained complete DMEM with 10% FBS. The cells in the upper layer of the filter membrane were gently wiped with cotton swabs after 8 h of culture. The cells on the other side were stained with crystal violet. Following the staining, the stained cells were examined under an optical microscope (IX73, Olympus, Japan) and counted using ImageJ software in five random microscopic fields.

### 2.5.4. Tube formation assay

A tube formation assay was performed with Matrigel matrix (Corning, USA) to detect the angiogenesis of HUVECs *in vitro* according to manufacturer's protocol. In briefly, HUVECs ( $1 \times 10^5$  cells/mL) were cocultured on scaffolds for 48 h and then resuspended and seeded on Matrigel surfaces. After culturing for 6 h, the cells were observed under an optical microscope (IX73, Olympus; Japan). The number of junctions and total length of tubes were calculated using ImageJ software.

### 2.5.5. Immunofluorescence staining

The proliferation ability of HUVECs was assessed by staining with 5-ethynyl-2'-deoxyuridine (EdU)/Hoechst 33,342 after 3 days of culturing on scaffold surfaces. Immunofluorescence staining of CD31 was accomplished by incubating the samples overnight at 4 °C with the primary antibody against CD31 and incubating the samples for 1 h with the fluorescent secondary antibody. The samples were then stained with FITC-phalloidin (green) for 60 min and DAPI (blue) for 10 min. Finally, CD31 expression was observed using a confocal laser scanning microscope (FV3000, Olympus, Japan).

### 2.5.6. Alkaline phosphatase activity assay

ALP activity of BMSCs was tested *in vitro* for osteoblastic differentiation ability. The cell culture method and seeding protocol were the same as those described above, except that the culture medium was replaced with an osteogenic medium containing 50  $\mu$ g/mL ascorbic acid (A4544; Sigma), 100 nM dexamethasone (HY-14648, MCE), and 10 mM  $\beta$ -glycerophosphate (HY-D0886; MCE) to induce osteogenic differentiation. BCIP/NBT Alkaline Phosphatase Color Development Kit (Beyotime; China) was used to stain the cells on scaffolds after 7 days of culturing. In addition, scaffolds were soaked in osteogenic medium for 7 days and stained to exclude non-specific ALP staining.

### 2.5.7. Western blotting

HUVECs or BMSCs were lysed in RIPA lysis buffer (Beyotime; China), and protein concentrations were quantified using the BCA Protein Assay Kit (Beyotime; China). Next, proteins were separated by 12% (w/v) gel electrophoresis, electro-transferred to polyvinylidene difluoride

membranes (Millipore, USA), and blocked in 5% (w/v) nonfat milk. The membranes were probed with the following primary antibodies at 4 °C overnight: YAP (1:1000), p-YAP (1:1000), TAZ (1:1000), p-TAZ (1:1000), OPN (1:1000), Runx-2 (1:1000) and  $\beta$ -actin (1:1000). The membranes were incubated with horseradish peroxidase-conjugated secondary antibodies for 2 h.

#### 2.5.8. qRT-PCR assay

The mRNA expression of several osteogenic genes, including Runx-2, OCN, and Col-1 were quantitatively determined by quantitative real-time PCR (qRT-PCR). Total RNA was extracted from cells grown on the scaffolds using the AG RNAex Pro Reagent (Accurate Biotechnology, China) seven days after scaffold addition. Reverse transcription was performed using the Evo M-MLV RT Mix Kit (Accurate Biotechnology, China) in T100™ Thermal Cycler (Bio-Rad, USA). mRNAs were quantified using the SYBR Green Premix Pro Taq HS qPCR kit (Accurate Biotechnology, China). qRT-PCR were performed using the BIO-RAD CFX384 (Bio-Rad, USA). The expression of osteogenic genes was normalized to GAPDH using the  $2^{-\Delta\Delta CT}$  method. Primer sequences were supplied in Table S1.

### 2.6. Bone regeneration and repair analysis in vivo

#### 2.6.1. Implantation surgery of scaffolds

Animal experiments were performed according to guidelines approved by the Zhejiang University Ethics Committee. Thirty-two male New Zealand white rabbits (2.5–3.0 kg) were divided randomly into three groups according to the pore geometries (cubic, cylindrical, and gyroid pore) of the bioceramic scaffolds. All scaffolds used here were designed as a cylindrical sample ( $\varnothing 6.0 \times 8.0$  mm). After general intravenous anesthesia with 3% pentobarbital sodium at 1.0 mg/kg, A critical size defect ( $\varnothing 6.0 \times 8.0$  mm) was constructed using a dental drill on the lateral condyle of the femur (see Scheme 1B) and then implanted a bioceramic sample. Penicillin (800,000 units) was injected intramuscularly 3 days after the operation to prevent postoperative infection. The rabbits were sacrificed at 1, 2, 4, 8, and 12 weeks after surgery, and femoral condyle specimens were collected.

#### 2.6.2. Surgery of vascular perfusion

Rabbits were perfused using Microfil (MV-122, Flow Tech Inc., USA) at 4 and 12 weeks after the implantation surgery to evaluate angiogenesis in the process of bone regeneration. In order to expose the abdominal aorta and inferior vena cava, the abdominal cavity was opened under anesthesia with 3% sodium pentobarbital (1.0 mg/kg). Two vessels were both intubated using infusion needles. Thereafter, heparinized normal saline, 10% formalin, and 60 mL mixed Microfil solution were perfused from the entrance (the abdominal aorta) to the outtrace (the inferior vena cava). The perfused rabbits were stored at 4 °C overnight to ensure polymerization of the contrast medium and the femur specimens were collected, decalcified and subjected to 2D&3D angiogenic reconstruction analysis using micro-computed scanner (Inveon, Siemens, Germany).

#### 2.6.3. Micro-CT scanning analysis

All specimens were scanned with a high-resolution micro-computed scanner (Inveon, Siemens, Germany). A volume of interest was defined as a cylindrical space ( $\varnothing 6.0$  mm  $\times$  8.0 mm) for the 3D histomorphometry evaluation. The structural images of new bones, new blood vessels and scaffolds were rebuilt and evaluated visually. In addition, morphological parameters were determined based on micro-CT data, including the fraction of bone volume/tissue volume (BV/TV), trabecular number (Tb.N), Trabecular spacing (Tb.Sp), trabecular thickness (Tb.Th), and vessel volume.

#### 2.6.4. Histological staining

Specimens for histological analysis were fixed in a 4% paraformaldehyde solution. The samples were dehydrated and embedded in methyl methacrylate (MMA) for undecalcified sectioning. Sections were

stained with McNeal staining and H&E staining and viewed by an optical microscope (IX73, Olympus, Japan).

### 2.7. Statistical analysis

One-way or two-way analysis of variance (ANOVA) was performed for statistical analysis and followed by Tukey's method to test all pairwise comparisons. All numerical data were expressed as the mean value  $\pm$  standard deviation (SD).  $P < 0.05$  was considered statistically significant. \* $P < 0.05$  and \*\* $P < 0.01$ .

## 3. Results

### 3.1. Characterization of bioceramic powders and scaffolds

The X-ray diffraction (XRD) patterns (Fig. S1; SI) confirmed that the powders exhibited the pure  $\beta$ -wollastonite phase according to the characteristic peaks with the PDF standard card (PDF#43-1460), and the incorporation of Mg and Sr did not change the crystalline phase. According to the inductively coupled plasma (ICP) analysis, the Mg and Sr contents in the CS powders were 6.93 mol% and 2.65 mol%, respectively, which was a little more or slightly lower than the theoretical determinations for the synthetic condition (Tab. S2). As shown by the 2D/3D models printed using 3D printing technology, the three groups of porous structures exhibited distinct topological structures. Observation of the Micro-CT reconstructions showed that each sintered scaffold demonstrated satisfactory pore connectivity in all directions (Fig. 1A–C). Meanwhile, the bioceramic scaffolds with different pore geometries showed similar macroscopic pore structures to its CAD model (Fig. 1D). Microscopically, the SEM images confirmed that the scaffolds exhibited the intrinsic pore geometries of cubic, cylindrical, and gyroid pores, and high-magnification SEM images also demonstrated the high sintering properties and densification of the pore walls (Fig. 1E). Moreover, after immersion in simulated body fluid (SBF), the pore surfaces showed apatite deposition, and the presence of this new biomimetic mineralization layer was confirmed by energy dispersive spectroscopy (EDS) and the appreciable amounts of phosphorus in the surface layer. However, the structural parameters showed minimal differences between the three groups of porous bioceramics, as shown in Fig. 1F. In particular, the gyroid pore scaffolds showed the highest porosity, pore diameters and specific surface areas, while the cylindrical pore scaffolds showed the greatest pore-wall thickness after undergoing sintering treatment (Table 1).

### 3.2. Mechanical properties and bio-dissolution behavior in vitro

To evaluate the structural stability and fracture strength of the scaffolds, an *in vitro* compression test was performed. The apparent compressive strength and Young's modulus of the scaffolds are shown in Fig. 2A&B. All scaffolds showed excellent mechanical performances in terms of strength, especially the cubic and cylindrical pore scaffolds ( $>25$  MPa). In contrast, the gyroid pore scaffolds showed higher Young's modulus values ( $\sim 736.50$  N/m<sup>2</sup>), indicating a greater anti-deformation properties. From the stress-strain curve presented in Fig. 2C, it can be seen that the three scaffold types all showed the typical brittle crushing properties of porous bioceramics with a sudden drop in the peak after isolation of the linear elastic regions. In addition, the degradation performance (bio-dissolution *in vitro*) and ion-release levels of the porous scaffolds were evaluated using an immersion test in Tris-HCl buffer. Interestingly, the cylindrical pore scaffolds showed a slower mass loss in the first eight weeks (Fig. 2D). After prolongation of the immersion time to 12 weeks, similar mass decay ( $\sim 8.0\%$ ) was observed for all scaffolds, irrespective of pore geometry. Moreover, in terms of ion release during the early stage (0–14 days; Fig. 2E), the concentrations of calcium, silicon, magnesium, and strontium ions increased rapidly during the initial 3–5 days, after which they either increased slowly or remained steady. It

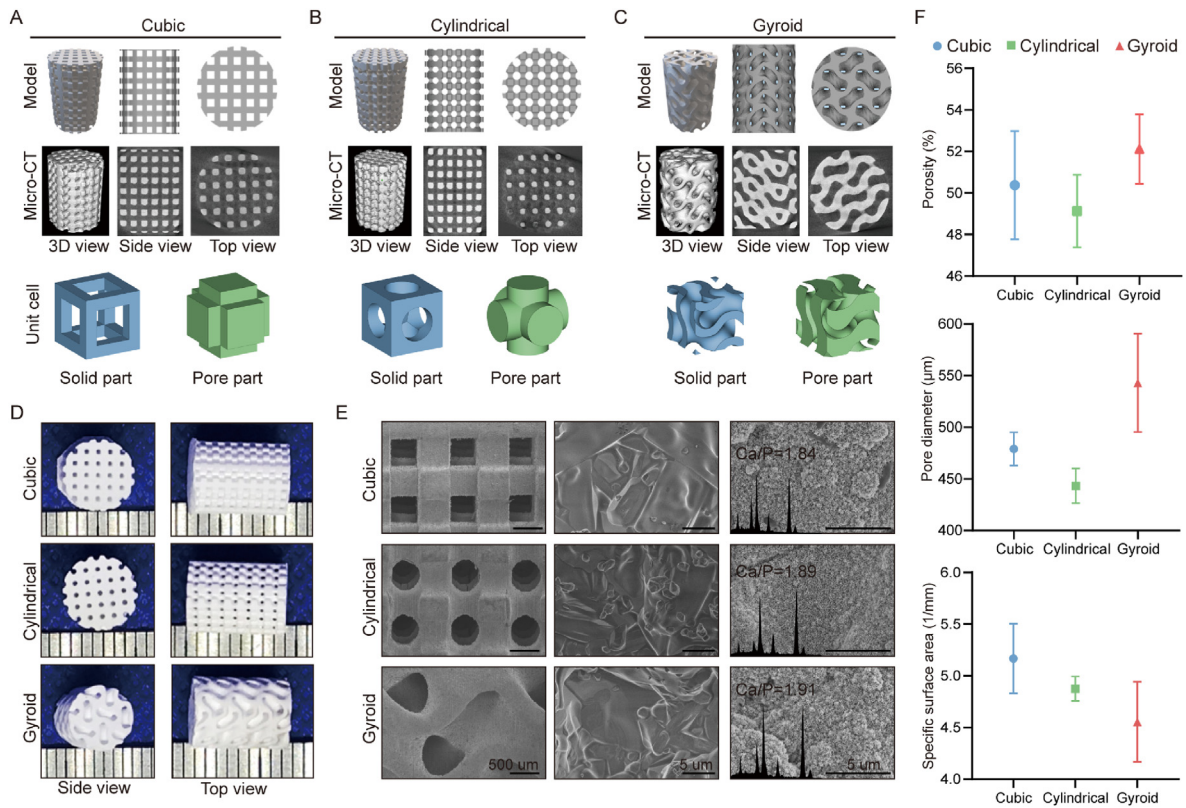


**Fig. 1.** Preparation and evaluation of wollastonite scaffolds. Theoretical models, reconstruction models by Micro-CT, and unit cells including solid parts (blue) and pore parts (green) with different pore morphologies of (A) Cubic, (B) Cylindrical, and (C) Gyroid. (D) External appearance of the scaffolds in side and top views. (E) Microstructures of scaffolds by SEM and the apatite coating soaked in SBF for 1 week. (F) Porosities, pore diameters, and specific surface areas calculated by Micro-CT. (For interpretation of the references to colour in this figure legend, the reader is referred to the Web version of this article.)

**Table 1**  
Geometrical parameters of the MS-CSi scaffolds.

Pore geometries	Theoretical pore size (μm)	Measured pore size (μm)	Theoretical porosity (%)	Measured porosity (%)	Theoretical specific surface area (1/mm)	Measured specific surface area (1/mm)
Cubic	600	445.62 ± 73.77	55	50.38 ± 3.61	7.66	4.82 ± 0.45
Cylindrical	600	443.13 ± 16.74	55	49.13 ± 1.75	6.53	4.74 ± 0.17
Gyroid	600	542.99 ± 47.61	55	52.12 ± 1.68	6.43	4.38 ± 0.38

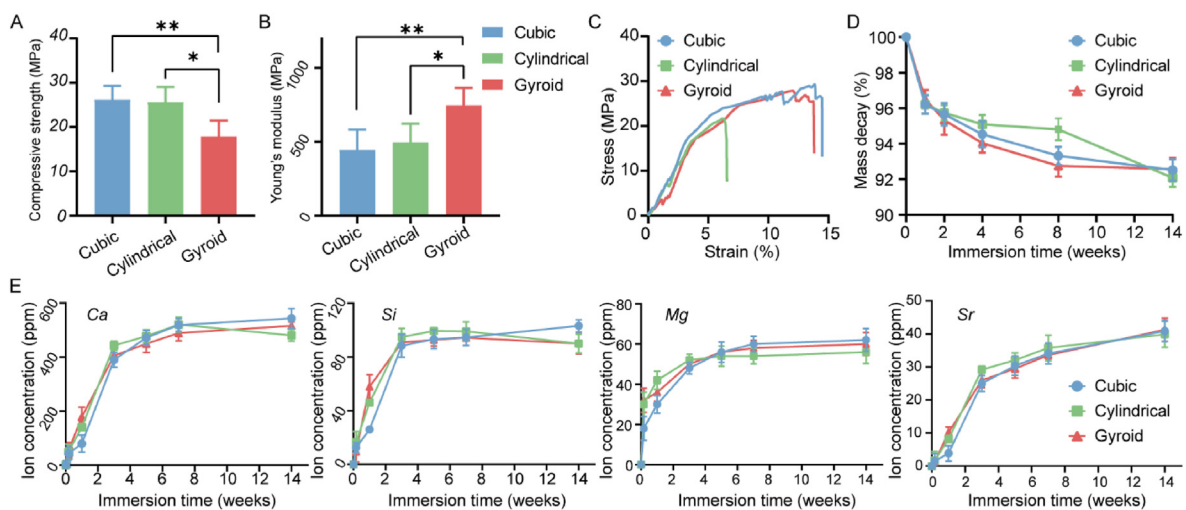


**Fig. 2.** The compressive strength (A) and young's modulus (B) of scaffolds (n = 3, \*p < 0.05, \*\*p < 0.01). (C) The representative the stress-strain curve of scaffolds. (D) The mass decay of scaffolds in Tris-HCl buffer for 12 weeks. (E) The ion release behavior of Ca, Si, Mg, and Sr from the scaffolds in Tris-HCl buffer for two weeks.

is worth mentioning that the early calcium and silicon ion release rates from the cubic pore scaffolds were slightly slower than that from the other scaffolds.

### 3.3. Evaluation of angiogenic capability *in vitro*

The HUVECs were cultured on the scaffolds for 1–7 days to evaluate the angiogenic cytocompatibility of the scaffolds. Cell proliferation analyzed using a CCK-8 kit (Fig. 3A) indicated that HUVECs in the porous bioceramics showed an appreciable proliferation during culture, without any cytotoxicity in comparison with the control group. Notably, cells grown on gyroid scaffolds showed the highest proliferation rate, implying that this pore architecture may effectively promote the growth of HUVECs. The ability of scaffolds to recruit HUVECs from the surrounding region was assessed by Transwell assays. As shown in Fig. 3B, the three groups of HUVECs exhibited better migration ability during the 8 h duration of the assay. In the control group, only a few cells migrated within 8 h in medium containing low serum concentrations. Quantification of the number of migrating cells (Fig. 3C) indicated that there were slightly more migrating HUVECs in the gyroid pore group than those in the other two types of pore scaffolds.

Fig. 3F shows a representative image of tube formation after incubation of HUVECs on Matrigel matrix for 6 h. Cells grown on gyroid scaffolds formed more networks than those in the other two groups. Quantitative analysis indicated that the total tube lengths and the numbers of junction points were significantly different between the cubic group and the other experimental groups (Fig. 3D). However, the total tube length was not significantly different between the gyroid and cylindrical pore groups (Fig. 3E). These results indicate that the bioceramic scaffolds, and especially those with the gyroid pore geometry, can significantly improve the angiogenic capability of HUVECs. To further verify the angiogenic properties of HUVECs cultured on different scaffolds, immunofluorescence staining for CD31 was performed. The HUVECs were cultured on scaffolds for 3 days and fluorescently labeled with red, green, and blue for CD31, actin, and nuclei, respectively. Immunofluorescence staining showed that the gyroid pore architecture could significantly enhance CD31 fluorescence in HUVECs compared to that in the other groups (Fig. 3G). Furthermore, we observed significantly increased proliferation of HUVECs demonstrated by the 5-ethynyl-2'-deoxyuridine (EdU) proliferation assay in the gyroid pore group compared with the other groups (Fig. 3H). Finally, the levels of YAP, p-YAP, TAZ, and p-TAZ protein expression were measured to assess the signaling of YAP/TAZ pathway. In the gyroid pore group, the levels of p-YAP and p-TAZ were significantly lower compared to the other groups (Fig. 3I).

### 3.4. Evaluation of osteogenic capability *in vitro*

Proliferation of BMSCs on the porous scaffolds *in vitro* was assessed using CCK-8 kit assays. As shown in Fig. 4A, all three groups showed significant osteogenic proliferation, with no significant differences observed between the groups. The alkaline phosphatase (ALP) level is an early-stage marker of BMSC differentiation into osteoblasts. Therefore, ALP levels were used to detect whether the scaffolds promoted osteogenesis in BMSCs. As shown in Fig. 4B, after seven days of induction, the BMSCs exhibited significantly higher ALP activity on the bioceramic scaffolds compared with cells in the Control group. To further verify the osteogenic potential of BMSCs after seven days of culture, the protein expression levels of OPN and Runx-2 were verified by Western blotting. Runx-2 is a transcription factor controlling the expression of genes involved in bone formation and plays an important role in controlling osteoblast differentiation. As shown in Fig. 4C, cell growth on the MS-CSi scaffolds increased the proteins levels of both OPN and Runx-2 in BMSCs and promoted their osteogenesis. Osteoblasts synthesize and secrete a variety of bone-specific marker proteins such as Runx-2, ALP, Col-1, and

OCN. Analysis of the expression of osteogenesis-related genes was performed using qRT-PCR. The expression levels of these genes in BMSCs cultured on the scaffolds for seven days were shown in Fig. 4D. The results showed that the mRNA levels of Col-1 and Runx-2 were upregulated in the three groups. In particular, the cylindrical pore group showed the highest levels of Col-1 and Runx-2 expressions while the OCN expression level was only upregulated in the cubic pore group.

### 3.5. Evaluation of angiogenic efficiency *in vivo*

Blood vessels were hardened by injection of Microfil-122 and can be recognized by Micro-CT (Fig. 5A). Micro-CT measurements were performed at 4 and 12 weeks postoperatively to evaluate new blood-vessel formation in the bone defects. The representative 2D/3D reconstructed images of neovascularization are shown in Fig. 5B. The neovessels were mainly small with most growing in the horizontal direction along the pore channels in the cubic and cylindrical pore groups after four weeks. In contrast, there was significantly more neovascularization visible in the gyroid pore group at four weeks, and probably because of the specific curvature of the gyroid pore structure, the ingrowth of the vessel was not hindered by the curved pore networks but filled the entire space inside the scaffold. At 12 weeks, the blood vessels in the bioceramic scaffolds covered the whole pores with significantly greater connectivity than before. There was obvious angiogenesis in the porous architectures. Furthermore, all scaffolds retained their pore constructs throughout the entire experiment, without any signs of structural collapse even after long-term culture. The quantitative analysis of neovascularization is shown in Fig. 5B. At four weeks, the volume of vessels in the gyroid pore group was significantly higher than that in the other two groups, reaching an average of 2.55 mm<sup>3</sup>. After 12 weeks, the vessel volumes in the gyroid and cylindrical pore groups (~2.9 mm<sup>3</sup> and ~2.78 mm<sup>3</sup>, respectively) were significantly higher than those in the cubic pore group ( $P < 0.05$ ) (Fig. 5C).

### 3.6. Evaluation of osteogenic efficiency *in vivo*

#### 3.6.1. 2D/3D reconstruction analysis

Critically sized femoral bone defects were constructed for the evaluation of the repair efficacy of the bioceramic scaffolds with different pore geometries (Scheme 1B). Micro-CT measurements were performed at 2, 4, 8, and 12 weeks postoperatively to evaluate the formation of new bone over time. As shown in the representative 2D/3D Micro-CT images in Fig. 6A, the new bone tissue grew readily into the deep layers of the pore networks over time. In particular, the new bone tissue was observed to grow into the macroporous networks of the cubic and cylindrical pore scaffolds within two weeks, while there were only limited amounts of new bone tissue in the peripheral pores of the gyroid pore scaffolds. However, there was obvious growth of bone tissue in all three groups after four weeks while appreciable amounts of new tissue had grown into the pore networks in all three scaffold types after eight weeks with indications of bone remodeling in the cubic and cylindrical pore scaffolds after 12 weeks. It is worth noting that the pore structures of the three scaffolds were maintained throughout the experiment.

Quantitative measurements of parameters, including BV/TV, Tb.N, Tb.Sp and Tb.Th for the bone defects were obtained by 3D Micro-CT reconstruction software in the rabbit bone defects (Fig. 6B). During the first eight weeks after surgery, greater levels of bone tissue growth were observed in the cubic and cylindrical pore scaffolds compared with the gyroid pore scaffold. Specifically, the values for these quantitative parameters, including BV/TV, Tb.N, Tb.Sp and Tb.Th, for the cubic and cylindrical pore scaffolds at 12 weeks were significantly lower than those at eight weeks, implying the occurrence of new bone remodeling during this stage. In contrast, the new bone tissue induced by the gyroid pore scaffold reached its highest level at this stage.

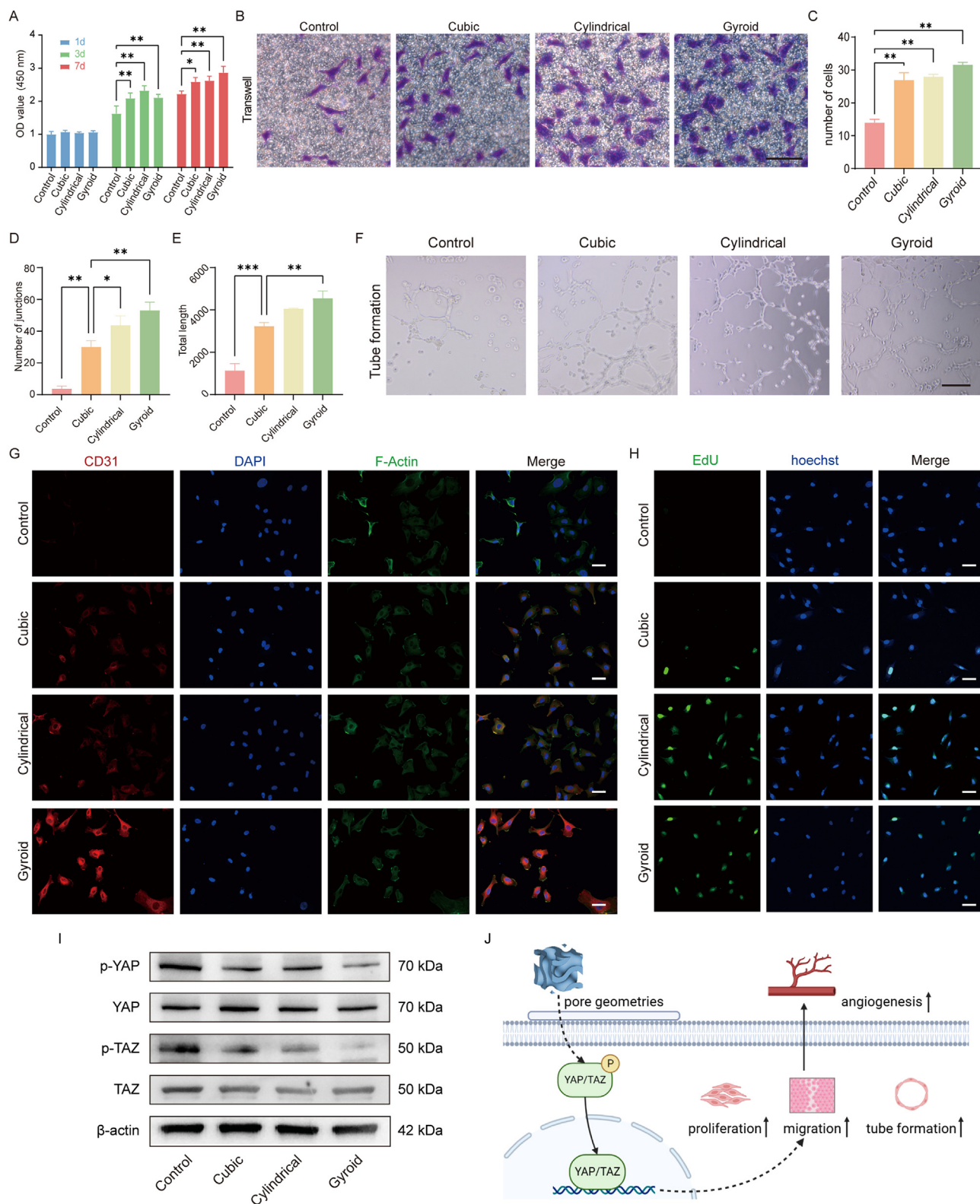


**Fig. 3.** The biocompatibility and angiogenesis capability of HUVECs on scaffolds. (A) Cell proliferation of HUVECs cultured on Gyroid, Cylindrical, Cubic, and Control evaluated by CCK-8 kit on days 1, 3, and 7. (B) Representative images of HUVECs (stained by crystal violet staining) migrating to the undersurface of upper chamber in Transwell system after culturing for 8 h. Scale bar = 100  $\mu$ m. (C) Quantitative analysis of the migrated cells in Transwell migration assay. The (D) number of junctions and (E) total length of tubes were statistically analyzed in the tube formation assay. (F) Representative images of tube formation after HUVECs cultured on Matrigel for 6 h. Scale bar = 200  $\mu$ m. Immunofluorescence staining of (G) CD31 and (H) EdU/Hoechst 33,342 after HUVECs were cultured on Gyroid, Cylindrical, Cubic, and Control for 3 days. Scale bar = 50  $\mu$ m. (I) Western blot images of p-YAP, YAP, p-TAZ and TAZ protein expression in HUVECs cultured on different scaffolds. (J) A schematic of the mechanism of pore geometry promoting angiogenesis through activation of the YAP/TAZ pathway. The control group received only the culture medium. Data represented as mean  $\pm$  SD (n = 3, \*p < 0.05, \*\*p < 0.01). (For interpretation of the references to colour in this figure legend, the reader is referred to the Web version of this article.)

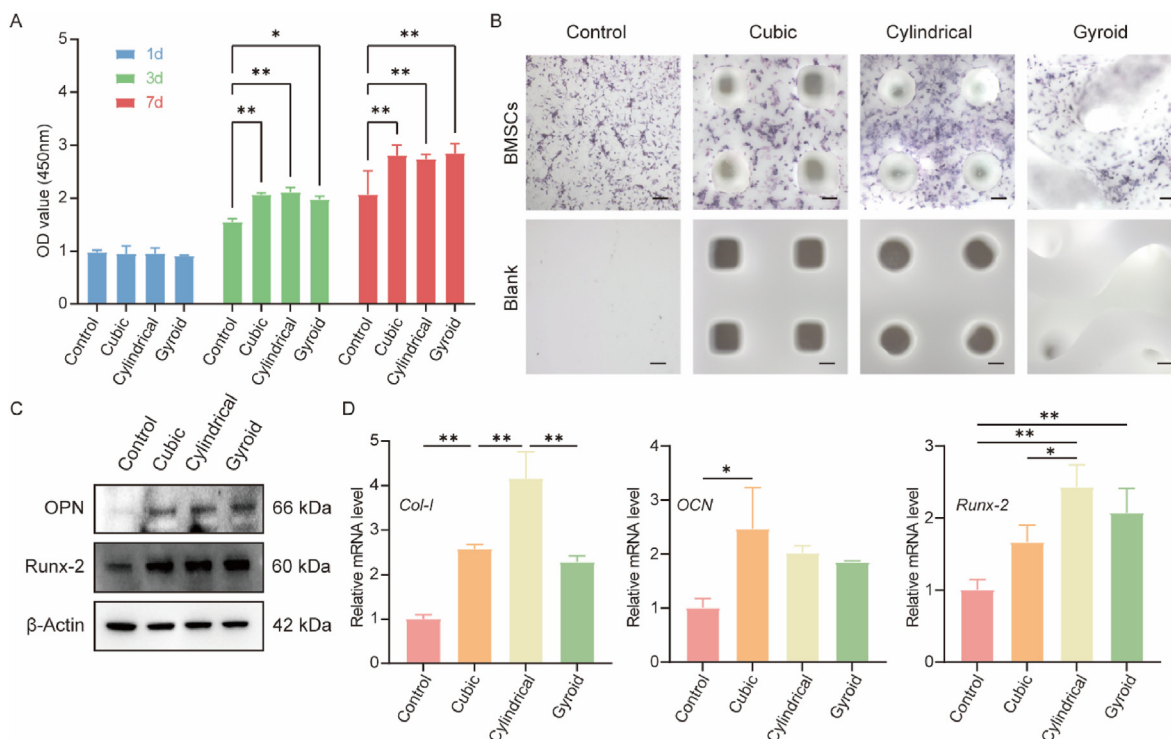


**Fig. 4.** The biocompatibility and osteogenic capability of BMSCs on scaffolds. (A) Cell proliferation of BMSCs cultured on Gyroid, Cylindrical, Cubic pore scaffolds and Control evaluated by CCK-8 kit on days 1, 3, and 7. (B) Representative ALP staining image of BMSCs cultured on Gyroid, Cylindrical, Cubic pore scaffolds and Control in the osteogenic medium after culturing for 7 days. Scale bar = 200  $\mu$ m. (C) Western blot images of OPN, and Runx-2 protein expression in BMSCs cultured on different scaffolds. (D) qRT-PCR analysis the relative mRNA expression levels of Col-1, OCN, and Runx-2 in BMSCs cultured on Gyroid, Cylindrical, Cubic pore scaffolds and Control for 7 days. The control group received only the culture medium. Data represented as mean  $\pm$  SD (n = 3, \*p < 0.05, \*\*p < 0.01).

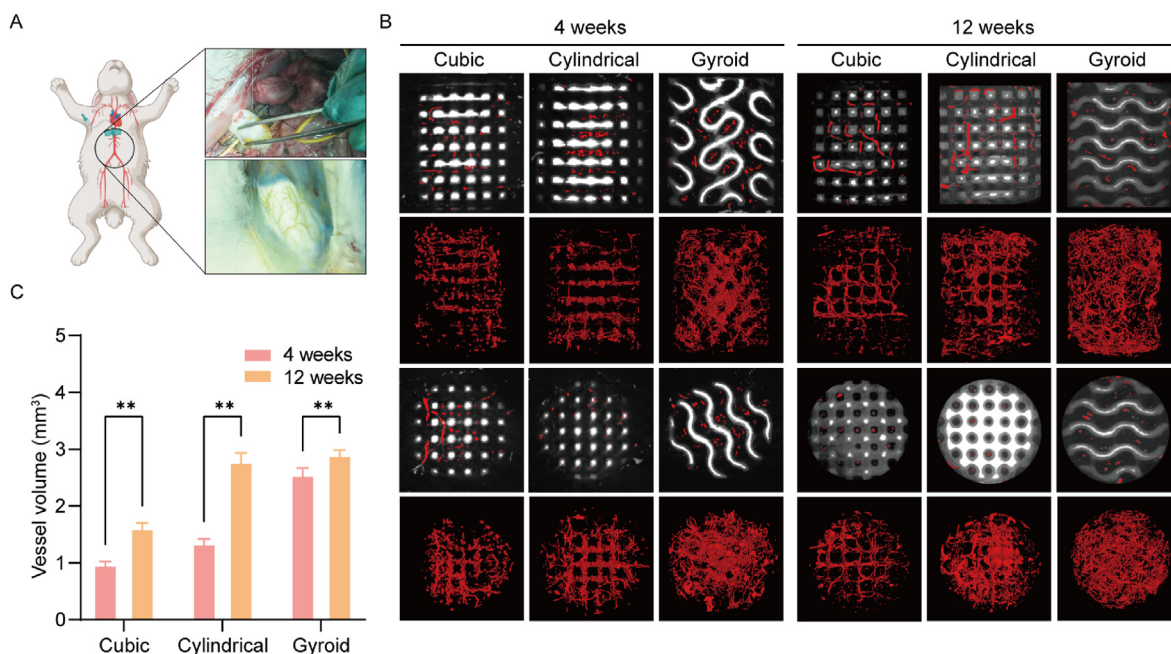


**Fig. 5.** (A) The process of angiography which realized by injection of microfil-122. (B) The representative 2D/3D reconstructed images of neovascularization at 4 and 12 weeks by Micro-CT measurement. (C) The quantitative analysis of neovascularization at 4 and 12 weeks (n = 3, \*\*p < 0.01).

### 3.6.2. Histological analysis

The purpose of the histological analysis was to examine the presence of osteogenesis in scaffolds with different pore geometries. Longitudinal sections of the bone specimens embedded with poly (methyl methacrylate) allowed easy observation of the scaffolds in the bone defects under

light microscopy. Images of McNeal stained sections showed that both the growth rate and degree of new bone formation differed between the bioceramic scaffolds (Fig. 7). In the early stage of new bone growth (2–4 weeks), the new bone tissue (deep-red color) was observed to have climbed from the peripheral pores into inner pore networks of the cubic

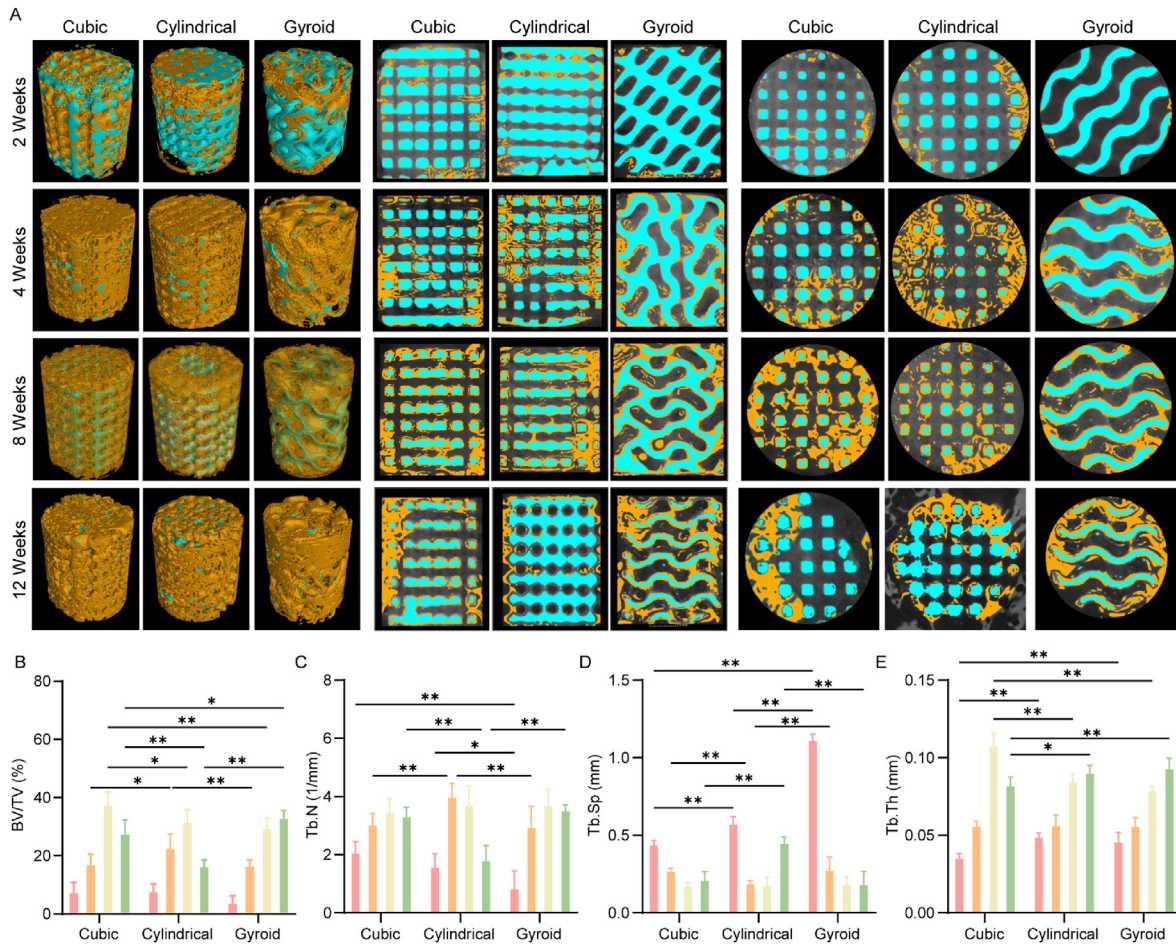


**Fig. 6.** (A) The representative 2D/3D reconstructed images of the bone defects at 2,4,8 and 12 weeks by Micro-CT measurements. (B) Bone volume/Total volume (BV/TV), Trabecular number (Tb.N), Trabecular Spacing (Tb.Sp), and Trabecular Thickness (Tb.Th) of the bone defects by 3D Micro-CT reconstruction software in the rabbit bone defects (Red: 2 weeks, Orange: 4 weeks; Yellow: 8 weeks, Green: 12 weeks). Data represented as mean  $\pm$  SD (n = 3, \*p < 0.05, \*\*p < 0.01). (For interpretation of the references to colour in this figure legend, the reader is referred to the Web version of this article.)

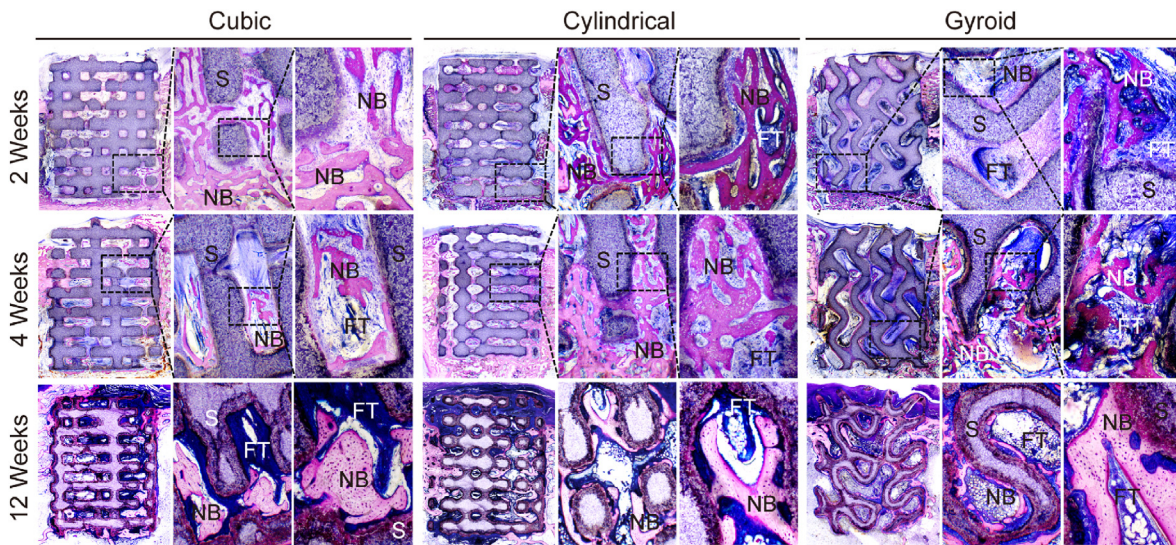


**Fig. 7.** McNeal-staining images of distal femur defects after with the implantation of three pore scaffolds (Cubic, Cylindrical, Gyroid) for 2, 4 and 12 weeks. (S, scaffolds; FT, fibrous tissue; NB, newly formed bone).

and cylindrical pore scaffolds but more fibrous tissue was observed in the gyroid pore group. After 12 weeks of new bone growth and

mineralization, the bone tissue in the cubic and cylindrical pore groups had entered the bone remodeling stage, and the mature bone tissue could

be seen as a light-red color. Furthermore, the histological analysis also confirmed that the porous architectures were well preserved after 12 weeks although the pore walls were thinner than those at two weeks. The newly formed bone tissue was expected to integrate with the bioceramic pore wall, which was also observed from the Micro-CT reconstructed 2D images.

The HE-stained images showed that the progress of vascularization and bone regeneration differed between the different pore geometries (Fig. 8). Inflammatory reactions were visible in the scaffolds after one week with large numbers of inflammatory cells observed from the high-magnification images as shown in Fig. 8B. A small amount of new bone tissue could be observed in the cubic and cylindrical pore groups after two weeks, while small numbers of new capillary vessels could be observed in gyroid pore group at the same time (Fig. 8C). In addition, it was confirmed that the gyroid pore architecture was advantageous for early vascularization and, furthermore, new bone tissue was only observed in the gyroid pore scaffolds after four weeks. Meanwhile, the new bone tissue had spread from the periphery of the pore to the center at eight weeks, and the gyroid pore networks were filled with new bone tissue and long strips of new blood vessels after 12 weeks (Fig. 8C).

#### 4. Discussion

Pore geometries are becoming increasingly relevant in the field of bone tissue repair using regenerative medicine techniques. In addition, researchers are aiming to develop structurally stable porous scaffolds with specifically optimized properties to promote and accelerate the regeneration of bone tissue [35,36]. The CAD-based additive

manufacturing techniques are highly effective for optimizing the external morphology and internal pore geometries of porous scaffolds [37]. Comparing pure CSI and M-CSI bioceramics, the present investigation demonstrated that MS-CSI is more effective for bone repair due to its appreciable mechanical strength and superior osteogenic activity. Pore geometries with TPMS types are newly developed topologies with mean curvatures of zero, as well as being infinite and periodic in 3D Euclidean space, rendering them highly controllable and homogeneous [38,39]. Natural systems such as sea urchins, corals, plant leaves, and the microstructures of mammalian trabeculae all have TPMS and similar geometrical features [40–42], possibly the result of the selection of such structures by convergent evolution [43]. For instance, gyroid pores have extensive specific surface areas, which are conducive to the migration of living cells and thus have good clinical potential [37]. Hence, such TPMS-typed porous scaffolds are expected to improve the osteoconductivity of biomedical materials, and thus provide a new prospect for the development of biodegradable ceramic scaffolds for bone repair. This study evaluated the mechanical properties and biodegradability of bioceramic scaffolds with different pore geometries. In addition, it explored the potential mechanisms by which the different pore geometries affected their osteogenic and angiogenic properties.

The XRD and ICP-OES analyses confirmed that the MS-CSI powders were free of any other secondary phase. It is reasonable to assume that increases or decreases in magnesium and strontium substitution may be attributable to the ionic diameters of these metal ions. The ionic diameters of magnesium, calcium, and strontium are increased, and hence the substitution of calcium ions by strontium is more difficult due to expansive type lattice deformation. In general, magnesium doping may

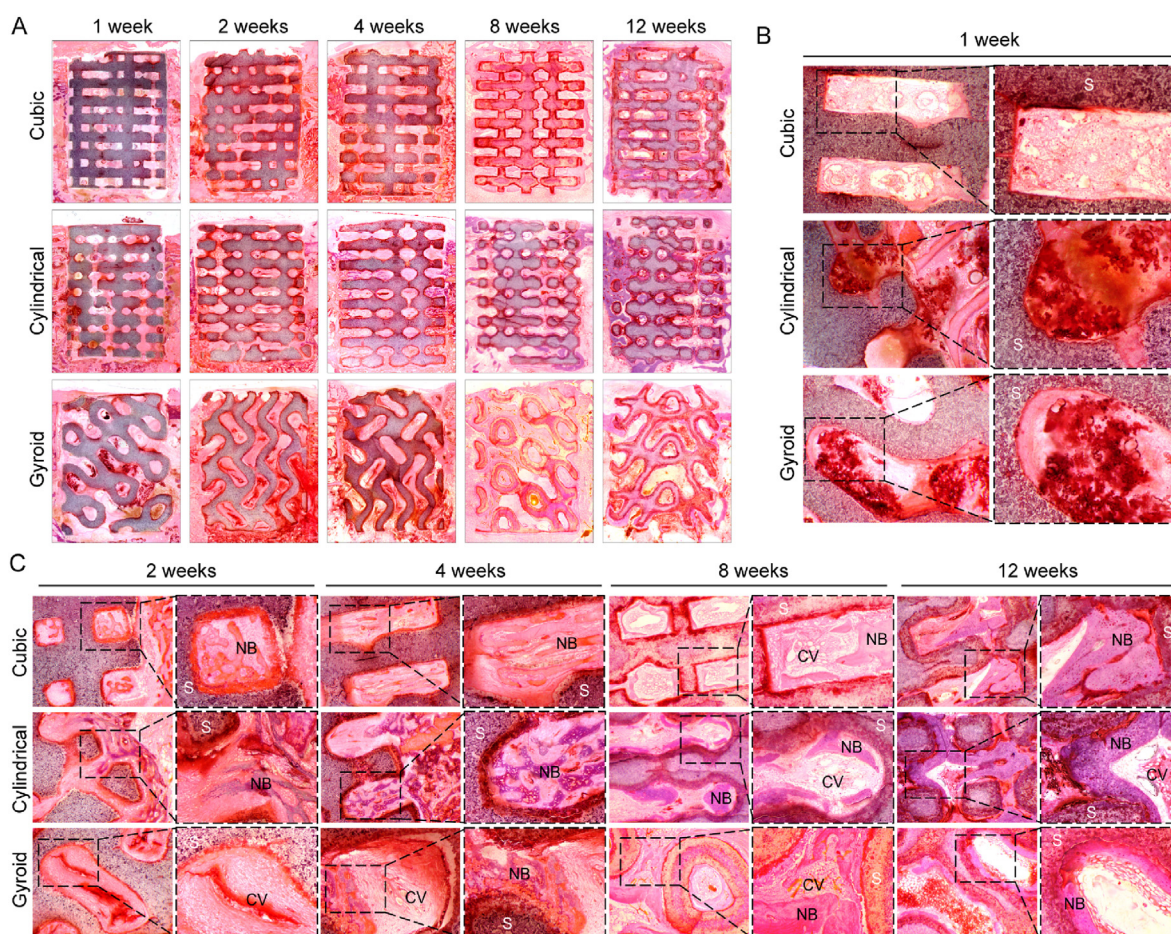


**Fig. 8.** The HE-staining images of distal femur defects after with the implantation of three pore scaffolds (Cubic, Cylindrical, Gyroid) *in vivo*. (A) The whole images for 1, 2, 4, 8, 12 weeks. The partial images for (B) 1 week and (C) 2, 4, 8, 12 weeks after implantation. (S: scaffolds, NB: new bone matrix, CV: capillary vessel).

significantly enhance the sintering properties of CSi bioceramics and the mechanical parameters can be improved [36]. Our previous study has showed that strontium doping of M-CSi led to mechanical decay as the strontium content increased [19]. Nevertheless, diluted doping of both magnesium and strontium in CSi bioceramics can still contribute an appreciable compressive resistance. In terms of the structural parameters, the real porosity of all scaffolds was ~50%, and the average pore size (~500  $\mu\text{m}$ ) are high enough for osteogenic cell migration and fibrous vascularization. The decreases in the structural parameters of the porous scaffolds are mainly ascribed to the high content of light-sensitive resin in the printing bodies and the inevitable linear shrinkage of the bioceramic during sintering [44]. It is evident that the similar porosity and pore sizes of the scaffolds with different pore geometries may be effective for ensuring constancy of structural conditions when evaluating angiogenesis and osteogenesis [45].

Ideally, porous scaffolds should have mechanical properties similar to those of natural bones during the entire process of tissue repair and regeneration, especially when the scaffold is to be implanted into a load-bearing site [46]. It is also imperative to match the degradation rate of the scaffolds with the rate of bone formation. This is because the regeneration process is usually prolonged and thus the scaffolds should be mechanically stable with relatively constant stiffness and strength [47]. It is estimated that human cancellous bone has a compressive strength of 2–21 MPa and the elastic modulus is in the range of 5–104 MPa [48,49]. It has been demonstrated that mechanical strength is directly related to the pore topologies of the bioceramic scaffolds. The conventional strut-based cubic and cylindrical pore architectures may contribute a stronger structural collapse resistance (by ~35%) in comparison with the gyroid pore architecture, whereas the later exhibits more appreciable structural transformation ability. In fact, gyroid pore scaffolds possess a relatively lower compressive strength (~17.8 MPa) than the other two groups of scaffolds (>25 MPa). There is a complex relationship between the curvature and complexity of the porous structure of bioceramic scaffolds and their mechanical strength.

On the other hand, the *in vitro* bio-dissolution performance of the bioceramic scaffolds during the early stage (14 days after surgery) may also display cytocompatibility, bioactivity, biodegradability and structural stability in the bone defect environment. Overall, all the scaffolds showed almost 4% mass decay with a burst release of Ca and Si within the first three days, after which the ions at all concentrations showed slow increase. Also, both Mg and Sr showed similar increases and maintenance to each other during the early stage. It was noted that the gyroid pore scaffolds showed a slightly faster mass decay in Tris-HCl buffer after 12 weeks, which may be related to the slightly higher specific surface area of its pore structure. However, the mass decay rates of the scaffolds *in vitro* slowed as expected with prolongation of the immersion time (Fig. 2D). This indicates that the poor dissolution property of the MS-CSi bioceramic is beneficial for its integration with the host bone tissue *in vivo*. These results indicate that the different pore geometries in the bioceramic scaffolds have limited influence on the rate of ion release due to similarities in their pore parameters. Alternatively, the ability of bioceramic scaffolds to form an apatite layer on the pore walls during SBF immersion *in vitro* can also predict their ability to bond with bone and their bioactivity *in vivo* [50]. The surfaces of the MS-CSi bioceramic scaffolds can readily induce biomimetic apatite deposition during immersion in SBF. Therefore, these material conditions involving similar pore walls and ion release characteristics are advantageous for studying the effect of pore geometries on angiogenesis and osteogenesis.

Bone is a highly vascularized tissue and angiogenesis plays a significant role in bone formation [51]. Rapid angiogenesis is an important stage of bone regeneration. The vascular network not only provides nutrients and oxygen for bone regeneration and removes bone residue but also recruits hematopoietic stem cells, bone cells, and immune cells [52]. The influence of the three kinds of scaffolds on HUVECs was analyzed by Transwell migration and tube-formation assays. The results showed that compared to the cubic and cylindrical pore scaffolds, the gyroid scaffold

enhanced both migration and tube formation in HUVECs. We further analyzed the upstream mechanisms by which pore structures guide endothelial cell maturation. YAP/TAZ, as sensors and mediators of mechanical cues instructed by the cellular microenvironment, can regulate endothelial cell proliferation, migration, and survival, thereby controlling angiogenesis, blood vessel barrier formation, and vascular remodeling [53]. Based on recent research findings, it has been reported that biomaterials can activate YAP/TAZ pathways to influence cellular behavior and guide the rational design of materials [54–56]. We found that the unique pore curvature of the gyroid scaffold activated the YAP/TAZ pathway, inhibited their phosphorylation, and enhanced nuclear translocation. It is speculated that the scaffold pore geometry mediates the behavior of HUVECs following the pathway as shown in Fig. 3J. This study identifies the importance of YAP/TAZ mechano-transduction in the scaffold pore geometry-HUVECs interaction. Moreover, upregulated expression of osteogenesis-related genes such as OCN, OPN, Runx-2, and Col-1 was observed in the cubic and cylindrical pore scaffolds in comparison with the gyroid pore scaffold *in vitro*. These findings were confirmed by subsequent *in vivo* experiments. Overall, the pore geometry of scaffolds plays a critical role in determining the osteogenic and angiogenic potential. Wu et al. found that pore geometry was more important for vascular formation in bioceramic scaffolds than pore size and that the traditional cube or hexagonal pore geometry was only beneficial to improve mechanical strength without being conducive to early angiogenesis [57]. Bidan et al. studied the behavior of cells on pores of different shapes including prismatic, square, and cross shapes, to predict the growth of bone matrix [58]. It was found that the initial rate of overall tissue deposition was twice as fast in cross-shaped pores than in square-shaped pores. It was thus suggested that optimization of the pore shape may improve the growth rate of bone tissue. Recent studies have shown that a specific vessel subtype, the type-H vessel, which was strongly positive for both CD31 and endomucin (EMCN), could orchestrate the coordination of angiogenesis and osteogenesis in bone remodeling [59]. The present study showed that the CD31 expression level in cells in the gyroid pore scaffold was significantly higher than that in the other groups. It may be that the specific curvature of the gyroid pore scaffold promotes the maturation of HUVECs and their transformation to type-H endothelial cell. In addition, the pore geometries of scaffolds may also affect cell-material interactions to modulate paracrine activity of BMSCs for vascularized bone regeneration. Arnal-Pastor et al. found that sponge-like scaffolds promoted greater cell organization into tubular-like structures than grid-like scaffolds because the paracrine signaling of stem cells significantly enhanced the activity of endothelial cells [60]. Qazi et al. found that simply optimizing the pore size of scaffolds could significantly enhance the paracrine activity of BMSCs to significantly promote both migration and tube formation in endothelial cells [61]. Lian et al. observed that by stimulating the paracrine effect of BMSCs through the design of scaffold pore geometry, the biomaterial significantly enhanced the immunomodulatory, angiogenic and osteogenic potential [62].

## 5. Conclusion

Overall, we developed highly bioactive ceramic scaffolds with different pore geometries using DLP printing. Optimization of the 3D porous models and sintering parameters allowed fine control of the pore wall curvature in the scaffold. Under similar pore structural parameters, the gyroid pore architecture exhibited lower compressive resistance than the strut-based scaffolds. However, such TPMS-based pore curvature was found to be more beneficial for the survival and proliferation of HUVECs and significantly enhanced both migration and tube formation by enhancing the YAP/TAZ pathway. In contrast, the strut-based porous scaffolds were slightly superior to osteogenic stem cells in osteogenic ability. Specifically, the rabbit femoral defect repair model demonstrated the superior performances of the cubic and cylindrical pore scaffolds in terms of new bone formation while analysis of vascular perfusion

demonstrated the significant potential of the gyroid pore architecture in promoting neovascularization. These findings suggest that the topological structures of bioceramic scaffolds could be further developed and improved by DLP-based 3D printing, which may improve the application potential of these biomaterials in bone regenerative medicine.

### Ethics approval and consent to participate

All animal experiments were implemented in accordance with guidelines approved by the Zhejiang University Ethics Committee.

### Consent for publication

Not applicable.

### Funding

The work was supported by Zhejiang Provincial Basic Public Welfare Research Program (LGF21H060006, LGF22E030002), National Natural Science Foundation of China (82172419, 81902225) and Zhejiang Provincial Natural Science Foundation of China (LQ20H060008, LQ23H150004, LZ22E020002).

### Authors' contributions

YFL and JFL contributed equally to this work. YFL and JFL designed the experiment, carried out the experiment and wrote the first draft of the manuscript. SJ, CZ, CCZ, and YJ carried out the experiment. JS, HZC, MHY, JYZ, and XYX analyzed the data. ZRG, SZX, MDS gave the final approval and supervised the project. All the authors discussed the results and commented on the manuscript. The authors read and approved the final manuscript.

### Declaration of competing interest

The authors declare that they have no known competing financial interests or personal relationships that could have appeared to influence the work reported in this paper.

### Data availability

Data will be made available on request.

### Acknowledgements

We thank the technical support (microscopy platform: Xingguang Liang, Fangjie Lu, Yahong Wu) by the core facility, Central Laboratory, the First Affiliated Hospital, Zhejiang University School of Medicine with the confocal laser microscopy and thank Jingyao Chen, Qiong Huang, Yajun Yu, Chengcheng Zhang from the core facility platform of Zhejiang University School of Medicine for their technical support.

### Appendix A. Supplementary data

Supplementary data to this article can be found online at <https://doi.org/10.1016/j.mtbio.2023.100667>.

### References

- [1] Y. Wang, H. Zhang, Y. Hu, Y. Jing, Z. Geng, J. Su, Bone repair biomaterials: a perspective from immunomodulatory, *Adv. Funct. Mater.* (2022), 2208639, <https://doi.org/10.1002/adfm.202208639>.
- [2] L. Che, Y. Wang, D. Sha, G. Li, Z. Wei, C. Liu, Y. Yuan, D. Song, A biomimetic and bioactive scaffold with intelligently pulsatile teriparatide delivery for local and systemic osteoporosis regeneration, *Bioact. Mater.* 19 (2023) 75–87, <https://doi.org/10.1016/j.bioactmat.2022.03.023>.
- [3] Y. Kang, L. Ren, Y. Yang, Engineering vascularized bone grafts by integrating a biomimetic periosteum and  $\beta$ -TCP scaffold, *ACS Appl. Mater. Interfaces* 6 (2014) 9622–9633, <https://doi.org/10.1021/am502056q>.
- [4] J. Wang, Y. Tang, Q. Cao, Y. Wu, Y. Wang, B. Yuan, X. Li, Y. Zhou, X. Chen, X. Zhu, C. Tu, X. Zhang, Fabrication and biological evaluation of 3D-printed calcium phosphate ceramic scaffolds with distinct macroporous geometries through digital light processing technology, *Regen. Biomater.* 9 (2022), rbac005, <https://doi.org/10.1093/rb/rbac005>.
- [5] Q. Zhang, L. Ma, X. Ji, Y. He, Y. Cui, X. Liu, C. Xuan, Z. Wang, W. Yang, M. Chai, X. Shi, High-strength hydroxyapatite scaffolds with minimal surface macrostructures for load-bearing bone regeneration, *Adv. Funct. Mater.* 32 (2022), 2204182, <https://doi.org/10.1002/adfm.202204182>.
- [6] H. Shao, X. Ke, A. Liu, M. Sun, Y. He, X. Yang, J. Fu, Y. Liu, L. Zhang, G. Yang, S. Xu, Z. Gou, Bone regeneration in 3D printing bioactive ceramic scaffolds with improved tissue/material interface pore architecture in thin-wall bone defect, *Biofabrication* 9 (2017), 025003, <https://doi.org/10.1088/1758-5090/aa663c>.
- [7] J.-W. Kim, B.-E. Yang, S.-J. Hong, H.-G. Choi, S.-J. Byeon, H.-K. Lim, S.-M. Chung, J.-H. Lee, S.-H. Byun, Bone regeneration capability of 3D printed ceramic scaffolds, *Int. J. Mol. Sci.* 21 (2020) 4837, <https://doi.org/10.3390/ijms21144837>.
- [8] M. Zhang, R. Lin, X. Wang, J. Xue, C. Deng, C. Feng, H. Zhuang, J. Ma, C. Qin, L. Wan, J. Chang, C. Wu, 3D printing of Haversian bone-mimicking scaffolds for multicellular delivery in bone regeneration, *Sci. Adv.* 6 (2020), <https://doi.org/10.1126/sciadv.aaz6725>.
- [9] J. Wang, C. Wang, K. Jin, X. Yang, L. Gao, C. Yao, X. Dai, J. He, C. Gao, J. Ye, P. Li, Z. Gou, Simultaneous enhancement of vascularization and contact-active antibacterial activity in diopside-based ceramic orbital implants, *Mater. Sci. Eng. C* 105 (2019), 110036, <https://doi.org/10.1016/j.msec.2019.110036>.
- [10] C. Prati, M.G. Gandolfi, Calcium silicate bioactive cements: biological perspectives and clinical applications, *Dent. Mater.* 31 (2015) 351–370, <https://doi.org/10.1016/j.dental.2015.01.004>.
- [11] C.-T. Wu, J. Chang, Silicate bioceramics for bone tissue regeneration, *J. Inorg. Mater.* 28 (2013) 29–39, <https://doi.org/10.3724/SP.J.1077.2013.12241>.
- [12] Z. Jin, R. Wu, J. Shen, X. Yang, M. Shen, W. Xu, R. Huang, L. Zhang, G. Yang, C. Gao, Z. Gou, S. Xu, Nonstoichiometric wollastonite bioceramic scaffolds with core-shell pore struts and adjustable mechanical and biodegradable properties, *J. Mech. Behav. Biomed. Mater.* 88 (2018) 140–149, <https://doi.org/10.1016/j.jmbbm.2018.08.018>.
- [13] J. Xie, X. Yang, H. Shao, J. Ye, Y. He, J. Fu, C. Gao, Z. Gou, Simultaneous mechanical property and biodegradation improvement of wollastonite bioceramic through magnesium dilute doping, *J. Mech. Behav. Biomed. Mater.* 54 (2016) 60–71, <https://doi.org/10.1016/j.jmbbm.2015.09.012>.
- [14] L. Liu, F. Yu, L. Li, L. Zhou, T. Zhou, Y. Xu, K. Lin, B. Fang, L. Xia, Bone marrow stromal cells stimulated by strontium-substituted calcium silicate ceramics: release of exosomal miR-146a regulates osteogenesis and angiogenesis, *Acta Biomater.* 119 (2021) 444–457, <https://doi.org/10.1016/j.actbio.2020.10.038>.
- [15] I. Mutreja, D. Kumar, K. Hogan, E. Campbell, K. Mansky, C. Aparicio, Strontium- and peptide-modified silicate nanostructures for dual osteogenic and antimicrobial activity, *Biomater. Adv.* 135 (2022), 212735, <https://doi.org/10.1016/j.bioadv.2022.212735>.
- [16] Y.-C. Chiu, M.-Y. Shie, Y.-H. Lin, A.K.-X. Lee, Y.-W. Chen, Effect of strontium substitution on the physicochemical properties and bone regeneration potential of 3D printed calcium silicate scaffolds, *Int. J. Mol. Sci.* 20 (2019) 2729, <https://doi.org/10.3390/ijms20112729>.
- [17] S. Wang, L. Liu, X. Zhou, D. Yang, Z. Shi, Y. Hao, Effect of strontium-containing on the properties of Mg-doped wollastonite bioceramic scaffolds, *Biomed. Eng. Online* 18 (2019) 119, <https://doi.org/10.1186/s12938-019-0739-x>.
- [18] Y.-H. Lin, A.K.-X. Lee, C.-C. Ho, M.-J. Fang, T.-Y. Kuo, M.-Y. Shie, The effects of a 3D-printed magnesium-/strontium-doped calcium silicate scaffold on regulation of bone regeneration via dual-stimulation of the AKT and WNT signaling pathways, *Biomater. Adv.* 133 (2022), 112660, <https://doi.org/10.1016/j.msec.2022.112660>.
- [19] Y. Li, R. Wu, L. Yu, M. Shen, X. Ding, F. Lu, M. Liu, X. Yang, Z. Gou, S. Xu, Rational design of nonstoichiometric bioceramic scaffolds via digital light processing: tuning chemical composition and pore geometry evaluation, *J. Biol. Eng.* 15 (2021) 1, <https://doi.org/10.1186/s13036-020-00252-3>.
- [20] R. Wu, Y. Li, M. Shen, X. Yang, L. Zhang, X. Ke, G. Yang, C. Gao, Z. Gou, S. Xu, Bone tissue regeneration: the role of finely tuned pore architecture of bioactive scaffolds before clinical translation, *Bioact. Mater.* 6 (2021) 1242–1254, <https://doi.org/10.1016/j.bioactmat.2020.11.003>.
- [21] K. Song, Z. Wang, J. Lan, S. Ma, Porous structure design and mechanical behavior analysis based on TPMS for customized root analogue implant, *J. Mech. Behav. Biomed. Mater.* 115 (2021), 104222, <https://doi.org/10.1016/j.jmbbm.2020.104222>.
- [22] J. Shi, L. Zhu, L. Li, Z. Li, J. Yang, X. Wang, A TPMS-based method for modeling porous scaffolds for bionic bone tissue engineering, *Sci. Rep.* 8 (2018) 7395, <https://doi.org/10.1038/s41598-018-25750-9>.
- [23] S. Ma, K. Song, J. Lan, L. Ma, Biological and mechanical property analysis for designed heterogeneous porous scaffolds based on the refined TPMS, *J. Mech. Behav. Biomed. Mater.* 107 (2020), 103727, <https://doi.org/10.1016/j.jmbbm.2020.103727>.
- [24] A. Yáñez, A. Cuadrado, O. Martel, H. Afonso, D. Monopoli, Gyroid porous titanium structures: a versatile solution to be used as scaffolds in bone defect reconstruction, *Mater. Des.* 140 (2018) 21–29, <https://doi.org/10.1016/j.matdes.2017.11.050>.
- [25] C.N. Kelly, A.S.P. Lin, K.E.H. Leguineche, S. Shekhar, W.R. Walsh, R.E. Guldborg, K. Gall, Functional repair of critically sized femoral defects treated with bioinspired titanium gyroid-sheet scaffolds, *J. Mech. Behav. Biomed. Mater.* 116 (2021), 104380, <https://doi.org/10.1016/j.jmbbm.2021.104380>.

- [26] Y. Jin, H. Kong, X. Zhou, G. Li, J. Du, Design and characterization of sheet-based gyroid porous structures with bioinspired functional gradients, *Materials* 13 (2020) 3844, <https://doi.org/10.3390/ma13173844>.
- [27] A. Yáñez, A. Herrera, O. Martel, D. Monopoli, H. Afonso, Compressive behaviour of gyroid lattice structures for human cancellous bone implant applications, *Mater. Sci. Eng. C* 68 (2016) 445–448, <https://doi.org/10.1016/j.msec.2016.06.016>.
- [28] L. He, X. Liu, C. Rudd, Additive-manufactured gyroid scaffolds of magnesium oxide, phosphate glass fiber and polylactic acid composite for bone tissue engineering, *Polymers* 13 (2021) 270, <https://doi.org/10.3390/polym13020270>.
- [29] M. Zhanmanesh, M. Varmazyar, H. Montazerian, Fluid permeability of graded porosity scaffolds architected with minimal surfaces, *ACS Biomater. Sci. Eng.* 5 (2019) 1228–1237, <https://doi.org/10.1021/acsbomaterials.8b01400>.
- [30] S.C. Kapfer, S.T. Hyde, K. Mecke, C.H. Arns, G.E. Schröder-Turk, Minimal surface scaffold designs for tissue engineering, *Biomaterials* 32 (2011) 6875–6882, <https://doi.org/10.1016/j.biomaterials.2011.06.012>.
- [31] H. Montazerian, M.G.A. Mohamed, M.M. Montazeri, S. Kheiri, A.S. Milani, K. Kim, M. Hoorfar, Permeability and mechanical properties of gradient porous PDMS scaffolds fabricated by 3D-printed sacrificial templates designed with minimal surfaces, *Acta Biomater.* 96 (2019) 149–160, <https://doi.org/10.1016/j.actbio.2019.06.040>.
- [32] B. Feng, M. Zhang, C. Qin, D. Zhai, Y. Wang, Y. Zhou, J. Chang, Y. Zhu, C. Wu, 3D printing of conch-like scaffolds for guiding cell migration and directional bone growth, *Bioact. Mater.* 22 (2023) 127–140, <https://doi.org/10.1016/j.bioactmat.2022.09.014>.
- [33] J. Wang, Y. Peng, M. Chen, X. Dai, L. Lou, C. Wang, Z. Bao, X. Yang, Z. Gou, J. Ye, Next-generation finely controlled graded porous antibacterial bioceramics for high-efficiency vascularization in orbital reconstruction, *Bioact. Mater.* 16 (2022) 334–345, <https://doi.org/10.1016/j.bioactmat.2021.12.028>.
- [34] F. Lu, R. Wu, M. Shen, L. Xie, M. Liu, Y. Li, S. Xu, L. Wan, X. Yang, C. Gao, Z. Gou, Rational design of bioceramic scaffolds with tuning pore geometry by stereolithography: microstructure evaluation and mechanical evolution, *J. Eur. Ceram. Soc.* 41 (2021) 1672–1682, <https://doi.org/10.1016/j.jeurceramsoc.2020.10.002>.
- [35] G.L. Koons, M. Diba, A.G. Mikos, Materials design for bone-tissue engineering, *Nat. Rev. Mater.* 5 (2020) 584–603, <https://doi.org/10.1038/s41578-020-0204-2>.
- [36] H. Qu, H. Fu, Z. Han, Y. Sun, Biomaterials for bone tissue engineering scaffolds: a review, *RSC Adv.* 9 (2019) 26252–26262, <https://doi.org/10.1039/C9RA05214C>.
- [37] J. Lv, W. Jin, W. Liu, X. Qin, Y. Feng, J. Bai, Z. Wu, J. Li, Selective laser melting fabrication of porous Ti6Al4V scaffolds with triply periodic minimal surface architectures: structural features, cytocompatibility, and osteogenesis, *Front. Bioeng. Biotechnol.* 10 (2022), 899531, <https://doi.org/10.3389/fbioe.2022.899531>.
- [38] H.N.S. Krishnamoorthy, Z. Jacob, E. Narimanov, I. Kretschmar, V.M. Menon, Topological transitions in metamaterials, *Science* 336 (2012) 205–209, <https://doi.org/10.1126/science.1219171>.
- [39] L. Han, S. Che, An overview of materials with triply periodic minimal surfaces and related geometry: from biological structures to self-assembled systems, *Adv. Mater.* 30 (2018), 1705708, <https://doi.org/10.1002/adma.201705708>.
- [40] M.F. Hochella, D.W. Mogk, J. Ranville, I.C. Allen, G.W. Luther, L.C. Marr, B.P. McGrail, M. Murayama, N.P. Qafoku, K.M. Rosso, N. Sahai, P.A. Schroeder, P. Vikesland, P. Westerhoff, Y. Yang, Natural, incidental, and engineered nanomaterials and their impacts on the Earth system, *Science* 363 (2019), eaau8299, <https://doi.org/10.1126/science.aau8299>.
- [41] K. Michielsen, D.G. Stavenga, Gyroid cuticular structures in butterfly wing scales: biological photonic crystals, *J. R. Soc. Interface* 5 (2008) 85–94, <https://doi.org/10.1098/rsif.2007.1065>.
- [42] H.-U. Nissen, Crystal orientation and plate structure in echinoid skeletal units, *Science* 166 (1969) 1150–1152, <https://doi.org/10.1126/science.166.3909.1150>.
- [43] Y. Yang, T. Xu, H.-P. Bei, L. Zhang, C.-Y. Tang, M. Zhang, C. Xu, L. Bian, K.W.-K. Yeung, J.Y.H. Fuh, X. Zhao, Gaussian curvature-driven direction of cell fate toward osteogenesis with triply periodic minimal surface scaffolds, *Proc. Natl. Acad. Sci.* 119 (2022), e2206684119, <https://doi.org/10.1073/pnas.2206684119>.
- [44] R. Zhou, Y. Wang, Z. Liu, Y. Pang, J. Chen, J. Kong, Digital light processing 3D-printed ceramic metamaterials for electromagnetic wave absorption, *Nano-Micro Lett.* 14 (2022) 122, <https://doi.org/10.1007/s40820-022-00865-x>.
- [45] S. Bose, M. Roy, A. Bandyopadhyay, Recent advances in bone tissue engineering scaffolds, *Trends Biotechnol.* 30 (2012) 546–554, <https://doi.org/10.1016/j.tibtech.2012.07.005>.
- [46] V.C. Mow, R. Huiskes (Eds.), *Basic Orthopaedic Biomechanics & Mechano-Biology, third ed.*, Lippincott Williams & Wilkins, Philadelphia, PA, 2005.
- [47] M. Frohlich, W. Grayson, L. Wan, D. Marolt, M. Drobnic, G. Vunjak-Novakovic, Tissue engineered bone grafts: biological requirements, tissue culture and clinical relevance, *Curr. Stem Cell Res. Ther.* 3 (2008) 254–264, <https://doi.org/10.2174/157488808786733962>.
- [48] G.K. Kouvidis, M.B. Sommers, P.V. Giannoudis, P.G. Katonis, M. Bottlang, Comparison of migration behavior between single and dual lag screw implants for intertrochanteric fracture fixation, *J. Orthop. Surg.* 4 (2009) 16, <https://doi.org/10.1186/1749-799X-4-16>.
- [49] M.B. Sommers, C. Roth, H. Hall, B.C.C. Kam, L.W. Ehmke, J.C. Krieg, S.M. Madey, M. Bottlang, A laboratory model to evaluate cutout resistance of implants for peritrochanteric fracture fixation, *J. Orthop. Trauma* 18 (2004) 361–368, <https://doi.org/10.1097/00005131-200407000-00006>.
- [50] H.-M. Kim, T. Himeno, T. Kokubo, T. Nakamura, Process and kinetics of bonelike apatite formation on sintered hydroxyapatite in a simulated body fluid, *Biomaterials* 26 (2005) 4366–4373, <https://doi.org/10.1016/j.biomaterials.2004.11.022>.
- [51] C. Feng, W. Zhang, C. Deng, G. Li, J. Chang, Z. Zhang, X. Jiang, C. Wu, 3D printing of Lotus root-like biomimetic materials for cell delivery and tissue regeneration, *Adv. Sci.* 4 (2017), 1700401, <https://doi.org/10.1002/advs.201700401>.
- [52] A. Grosso, M.G. Burger, A. Lunger, D.J. Schaefer, A. Banfi, N. Di Maggio, It takes two to tango: coupling of angiogenesis and osteogenesis for bone regeneration, *Front. Bioeng. Biotechnol.* 5 (2017) 68, <https://doi.org/10.3389/fbioe.2017.00068>.
- [53] G.T.K. Boopathy, W. Hong, Role of hippo pathway-YAP/TAZ signaling in angiogenesis, *Front. Cell Dev. Biol.* 7 (2019), <https://doi.org/10.3389/fcell.2019.00049>.
- [54] G. Brusatin, T. Panciera, A. Gandin, A. Citron, S. Piccolo, Biomaterials and engineered microenvironments to control YAP/TAZ-dependent cell behaviour, *Nat. Mater.* 17 (2018) 1063–1075, <https://doi.org/10.1038/s41563-018-0180-8>.
- [55] W.B. Swanson, M. Omi, S.M. Woodbury, L.M. Douglas, M. Eberle, P.X. Ma, N.E. Hatch, Y. Mishina, Scaffold pore curvature influences MSC fate through differential cellular organization and YAP/TAZ activity, *Int. J. Mol. Sci.* 23 (2022) 4499, <https://doi.org/10.3390/ijms23094499>.
- [56] Z. Xu, J.A. Orkwis, G.M. Harris, Cell shape and matrix stiffness impact schwann cell plasticity via YAP/TAZ and rho GTPases, *Int. J. Mol. Sci.* 22 (2021) 4821, <https://doi.org/10.3390/ijms22094821>.
- [57] F. Wu, J. Yang, X. Ke, S. Ye, Z. Bao, X. Yang, C. Zhong, M. Shen, S. Xu, L. Zhang, Z. Gou, G. Yang, Integrating pore architectures to evaluate vascularization efficacy in silicate-based bioceramic scaffolds, *Regen. Biomater.* 9 (2022), <https://doi.org/10.1093/rb/rbab077>.
- [58] C.M. Bidan, K.P. Kommareddy, M. Rumpler, P. Kollmannsberger, P. Fratzl, J.W.C. Dunlop, Geometry as a factor for tissue growth: towards shape optimization of tissue engineering scaffolds, *Adv. Healthc. Mater.* 2 (2013) 186–194, <https://doi.org/10.1002/adhm.201200159>.
- [59] Y. Peng, S. Wu, Y. Li, J.L. Crane, Type H blood vessels in bone modeling and remodeling, *Theranostics* 10 (2020) 426–436, <https://doi.org/10.7150/thno.34126>.
- [60] M. Arnal-Pastor, C. Martínez-Ramos, A. Vallés-Lluch, M.M. Pradas, Influence of scaffold morphology on co-cultures of human endothelial and adipose tissue-derived stem cells, *J. Biomed. Mater. Res. A* 104 (2016) 1523–1533, <https://doi.org/10.1002/jbm.a.35682>.
- [61] T.H. Qazi, L. Tytgat, P. Dubruel, G.N. Duda, S. Van Vlierberghe, S. Geissler, Extrusion printed scaffolds with varying pore size as modulators of MSC angiogenic paracrine effects, *ACS Biomater. Sci. Eng.* 5 (2019) 5348–5358, <https://doi.org/10.1021/acsbomaterials.9b00843>.
- [62] M. Lian, B. Sun, Y. Han, B. Yu, W. Xin, R. Xu, B. Ni, W. Jiang, Y. Hao, X. Zhang, Y. Shen, Z. Qiao, K. Dai, A low-temperature-printed hierarchical porous sponge-like scaffold that promotes cell-material interaction and modulates paracrine activity of MSCs for vascularized bone regeneration, *Biomaterials* 274 (2021), 120841, <https://doi.org/10.1016/j.biomaterials.2021.120841>.